2023 IEEE International Conference on Robotics and Automation (ICRA 2023)
May 29 - June 2, 2023. London, UK

Control of Shape Memory Alloy Actuator via Electrostatic Capacitive Sensor for Meso-scale Mirror Tilting System

Baekgyeom Kim[1], Doohoe Lee[1], Dongjin Kim[1], Seungyong Han[1], Daeshik Kang[1], Uikyum Kim[1], and Je-sung Koh[1]

***Abstract*— Shape memory alloy (SMA) has superior actuation capability over the limit of the scale. However, inherently low controllability is a primary issue that hinders practical usage. To address this challenge, this paper presents an SMA-based artificial muscle actuator capable of the displacement sensing through the capacitive sensor. To realize sensing capability, the theoretical model-based design and fabrication process are proposed. Here, we show that the actuator can be controlled at intervals of 100 μm as well as maintaining sensing capability while lifting 90 times heavier than its weight. To exhibit the usefulness of the actuator to an optical device, we integrate the actuator into the mirror tilting device, which has 20 degrees tilting angle. We expect that the proposed actuator can overcome the scale limit of meso-scale devices, which require payload capacity and controllability, simultaneously.**

I. INTRODUCTION

An artificial muscle actuator has been consistently developed to overcome engineering limits over the past decade. These actuators can reduce the complexity of the mechanical system by utilizing characteristics such as compliance, a high power-to-weight ratio, a high force-to-weight ratio, and deforming their shape by external stimuli [1]. Through these advantages, artificial muscle actuators enable a substitute for conventional actuators (e.g., electric motor and hydraulic actuator) in specific applications including bio-inspired robots, soft robots, medical devices, and wearable devices [2]–[7]. The high power-to-weight ratio of artificial muscle actuators is a favorable characteristic that can decrease the scale of systems or devices [1]. Shape memory alloy (SMA) [7], dielectric elastomer (DE) [8], and piezoelectric transducer (PZT) [9] are representative materials to be exploited as the actuator. Unlike other types of artificial muscle actuators, SMA has a high force-to-weight ratio beyond the limitation of scale despite comparatively low actuation frequency. The core of this work is to improve controllability for a practical application, which can be hardly achieved by an SMA-based artificial muscle actuator while retaining its high force-to-weight ratio.

The SMA has been widely employed for decades in aerospace [10], automotive [11], robotic [1], and biomedical [12] applications due to its material property such as the shape memory effect through phase transformation induced by physical stimuli (e.g., thermal and mechanical), biocompatibility, and super-elasticity [12], [13]. Furthermore, the SMA has one of the highest energy density (10 J/cm^3) that enable lifting 100 times heavier than its weight [12]. This suggests that the SMA can significantly reduce the mechanical complexity and weight of the system. A low strain of the SMA (3-5 %) is a well-known disadvantage, but this can be addressed by forming the raw material into a spiral shape [14] or employing a strain-amplification mechanism with the compliant structure [7]. Additionally, low energy efficiency is also an issue as SMA is used for the actuator. However, the weight of the SMA wire embedded into the actuator is sub-milligrams in this work, which means

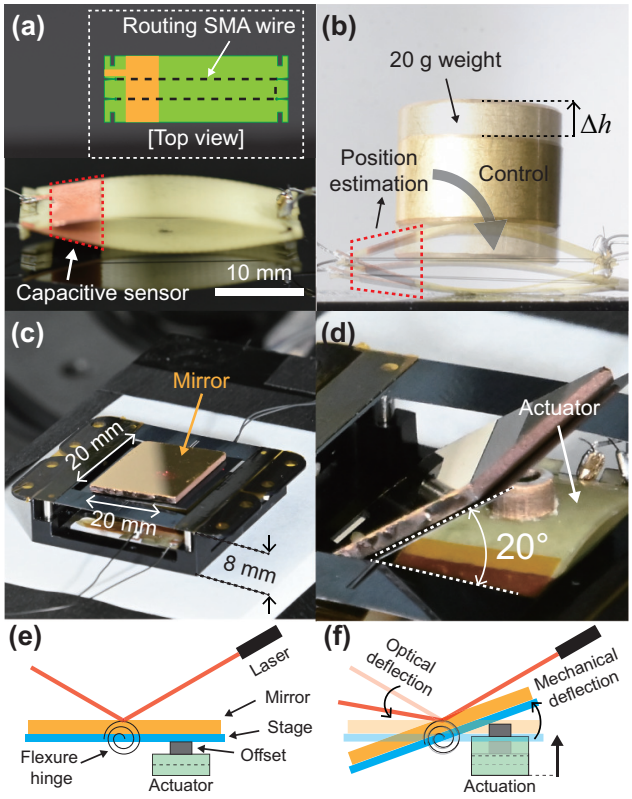

Fig. 1. Proposed actuator and device. (a) SMA-based artificial muscle actuator with integrated capacitive sensor and top view schematic diagram. (b) Control of the actuator through position sensing while lifting 20 g payload. (c) 1-DoF mirror tilting device with the rotational state. (d) Closeup image of mirror tilting device, showing maximum tilting angle. (e) Schematic diagram showing components of the mirror tilting device. (f) Mechanism of the laser steering.

This work was supported by Basic Science Research Program through the National Research Foundation of Korea (NRF-2021R1C1C1011872). *(Corresponding author: Uikyum Kim and Je-sung Koh)*

[1]The authors are with the Multiscale Bio-inspired Technology Lab, Mechanical Engineering, Ajou University, Suwon, Korea www7541@ajou.ac.kr; sktd4@ajou.ac.kr; rlaehdwlswt@ajou.ac.kr; sy84han@ajou.ac.kr; dskang@ajou.ac.kr; ukim@ajou.ac.kr; jskoh@ajou.ac.kr

the absolute value of energy consumption is small.

Nevertheless, the inherent limitation of the SMA interrupting usage as practical applications is low controllability resulting from non-linearity and hysteresis caused by temperature- and stress-induced phase transformation [13]. Theoretical modeling, control technique, and feedback sensor have been considered to address this challenge of the SMA actuator. For instance, the typical approach is strain estimation by measuring the temperature and electric resistance of the material itself [15]. Furthermore, measurement of SMA's temperature and resistance enables the feedback control of the SMA-based actuator without an additional bulky sensor [12]. However, these types of feedback control accompany a limited accuracy of the control due to the thermomechanical behavior of the SMA by phase transformation. Therefore, independently measured physical quantity is required to control the SMA actuator such as the optical pulse signal of the encoder for the motor control. Here, we present electrostatic capacitive sensing, which enables integration into the SMA-based artificial muscle actuator.

Electrostatic capacitive sensing is a convenient method for detecting contact or measuring the distance between objects. It is widely used for the touch interaction of most electronic devices including touch displays. Furthermore, capacitive sensors have a number of useful features for engineering applications: simple fabrication process to require only one or two electrodes; sensing capability in mechanically harsh environments such as flexible and stretchable electronics involving large deformation [16]; scalability to integrate sensor arrays into fingertip-size substrate [17]. In particular, the measured capacitance data can be easily transformed into other physical quantities such as displacement and force through theoretical modeling and experimental calibration [18]. Finally, the capacitive sensor provides high sensitivity to small displacement with low effect by temperature [19]. These advantages are favorable characteristics to integrate additional sensing functionality into the actuator system without increasing weight, volume, and complexity.

In this paper, we propose the SMA-based artificial muscle actuator with a self-displacement sensing function through electrostatic capacitive sensing (Fig. 1a). Actuator system in this work shows being capable of position control (100 μm step and sinusoidal response) through the low-profile capacitive sensor as well as maintaining high power-to-weight ratio and payload capacity (0.22 g weight of the actuator and 20 g payload), which is the primary advantage of SMA actuator (Fig. 1b). To evaluate controllability and applicability of this actuator, we devised 1-degree of freedom (DoF) mirror tilting device as shown in Fig. 1c. The device can tilt mirror (2×2 cm) approximately maximum 20 degrees as shown in Fig. 1d. In addition, the controllability was confirmed 100 μm step and sinusoidal response through demonstration of the laser beam steering as shown in Fig. 1e and 1f. We expect that the SMA-based artificial muscle actuator with integrated sensors in this work will be available in many applications that simultaneously require high payload capacity and control in centimeter-scale mechanical systems by improving the controllability of the SMA actuator.

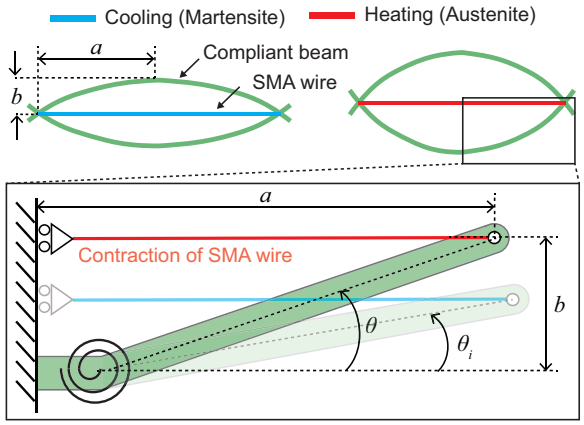

Fig. 2. Actuation mechanism and kinematic diagram of the actuator.

II. DESIGN & FABRICATION

A. Previous research and purpose of design

In a previous study, we developed a lightweight and thin multi-functional shape memory alloy-based actuator, which is applicable to various types of wearable devices [7]. Despite its superior performance regarding power-to-weight ratio and force sensing capability, the feedback system through the sensor should be taken into account for realizing precise position control of the actuator. Here, we contribute improvements: (1) easily integrating a thin-film sensor into the artificial muscle actuator; (2) estimating the position of the actuator by the mathematical model of the electrostatic capacitance.

B. Kinematic configuration of the actuator

The actuator which has an elliptic configuration consists of two compliant beams and an SMA wire as shown in Fig. 2. The ratio of the length of the compliant beam over the length of the SMA wire determines the initial configuration of the actuator [7]. We consider a quarter model for kinematic configuration because both buckled structures are two-axis symmetry. The initial configuration of the actuator can be calculated by a Pseudo-Rigid-Body (PRB) model as follows [20]:

$$\frac{b_i}{l} = \frac{1}{\kappa_0}\left(1-\cos\frac{\kappa_0}{2}\right), \tag{1}$$

$$\frac{a_i}{l} = \frac{2}{\kappa_0}\sin\frac{\kappa_0}{2} \tag{2}$$

where l is the length of the compliant beam, κ_0 is the curvature factor of the PRB model, and a_i and b_i are the initial horizontal and vertical displacement of the actuator, respectively.

As shown in Fig. 2, the initial PRB angle (θ_i) is expressed by the following equations.

$$\theta_i = \tan^{-1}\frac{b_i}{a_i - l(1-\gamma)} \tag{3}$$

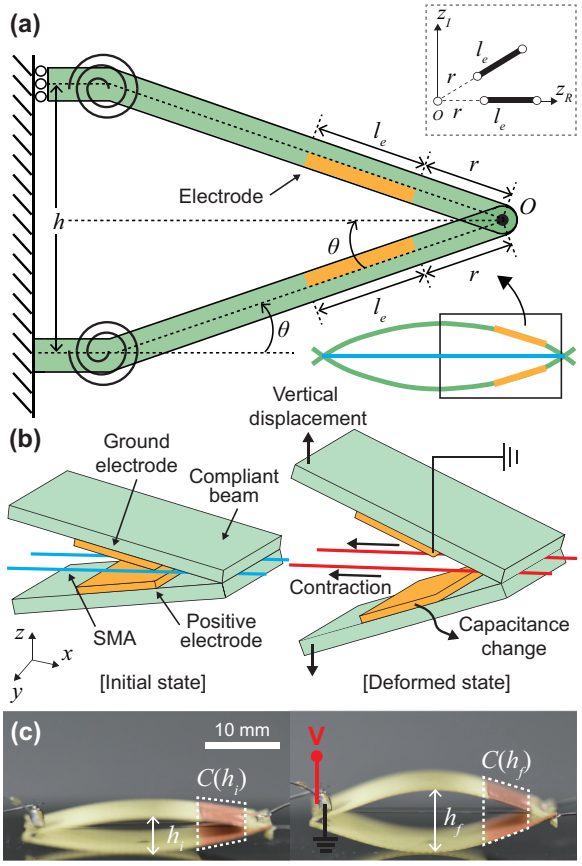

Fig. 3. Principles of design, actuation, and sensing mechanism. (a) Schematic diagram showing design parameter of a capacitive sensor coupled with two compliant beams (b) Mechanism of actuation and sensing. (c) Optical images showing the change of vertical displacement.

where γ is the radius factor of the PRB. The kinetic configuration of the compliant beam change depending on the PRB angle (θ) as follows:

$$a(\theta) = l\,(1-\gamma+\rho\cos\theta)\,, \tag{4}$$

$$b(\theta) = \frac{\rho l \sin\theta}{2} \tag{5}$$

where $a(\theta)$ and $b(\theta)$ represent horizontal and vertical displacement of the compliant beam depending on PRB angle (θ). Therefore, we can estimate the trajectory of the endpoint of the compliant beam by varying θ corresponding deflection path of the initially curved beam.

C. Principles of Capacitive sensing

The electrostatic capacitance change has been exploited for measuring force or displacement [18]. The capacitive sensor consists of two conductive plates and the dielectric material which is filled between two plates. Generally, the capacitance between two parallel electrodes changes to be dependent on the area of the electrode and displacement between two electrodes as follows:

$$C = \varepsilon_0 \varepsilon_r \frac{A}{d} \tag{6}$$

where C is the electrostatic capacitance. ε_0 and ε_r are the vacuum and relative permittivity, respectively.

To integrate sensing functionality into the actuator, we consider two inclined electrodes laminated on compliant beams as shown in Fig. 3a. In this kinematic configuration, the fringing effect is exploited to analyze the capacitance between two inclined electrodes. The variation of the capacitance depends on various parameters including the length of the electrode and the angle between two electrodes as denoted in Fig. 3a. Consequently, the height of the actuator can be estimated from the capacitance change.

Prior to deriving the mathematical model of inclined electrodes, we investigate the suitable location of the electrode layer on the compliant beam. The SMA wire embedded in the actuator is contracted by Joule heating, and then the horizontal contraction of the SMA wire induces vertical deformation of the compliant beam (i.e., half of the actuation displacement) as shown in Fig. 2. When the SMA wire actuates compliant beams, the beam is locally deformed near the fixed-end with curvature change (Fig. 2). This region is not suitable for attaching electrode: (1) the stress concentration by local deformation can cause the failure of the electrodes; (2) the fixed-end of the compliant beam involves the largest actuation displacement in the entire structure. the electrode or electric wire for data acquisition can disrupt the task of the actuator (e.g., object lifting); (3) definitely, the mechanical contact between electrode and object for the task deteriorates sensing performance by contact noise.

In contrast, the intersection point of compliant beams has a rotational DoF as a revolute joint (Fig. 3a). The side region of the compliant beam maintains a relatively planar configuration. Therefore, we design the capacitance model based on the kinematic configuration resulting from the PRB model (Section. II.B). The capacitance variation between two inclined electrodes can be derived as follows [21]:

$$\begin{aligned}\Delta C(\theta) &= C(\theta_0) - C(\theta) \\ &= [C_{in}(\theta_0) + C_{out}(\theta_0)] - [C_{in}(\theta) + C_{out}(\theta)]\end{aligned} \tag{7}$$

where

$$C(\theta) = C_{in}(\theta) + C_{out}(\theta), \tag{8}$$

$$C_{in}(\theta) = \frac{K'\left(k_{\text{in}}(\theta)\right)}{K\left(k_{\text{in}}(\theta)\right)}, \tag{9}$$

$$C_{out}(\theta) = \frac{K'\left(k_{\text{out}}(\theta)\right)}{K\left(k_{\text{out}}(\theta)\right)} \tag{10}$$

where $C(\theta)$ is the capacitance per unit longitudinal length depending on the PRB angle (θ), $K(k)$ is the complete elliptic integral of the first kind. The modulus k_{in} and k_{out} (i.e., function of angle, θ) are:

$$k_{in}(\theta) = \sqrt{\frac{4(r^2+rl_e)^{\pi/2\theta}}{\left(r^{\pi/2\theta}+(r+l_e)^{\pi/2\theta}\right)^2}}, \tag{11}$$

$$k_{out}(\theta) = \sqrt{\frac{4(r^2+rl_e)^{\pi/2(\pi-\theta)}}{\left(r^{\pi/2(\pi-\theta)}+(r+l_e)^{\pi/2(\pi-\theta)}\right)^2}} \tag{12}$$

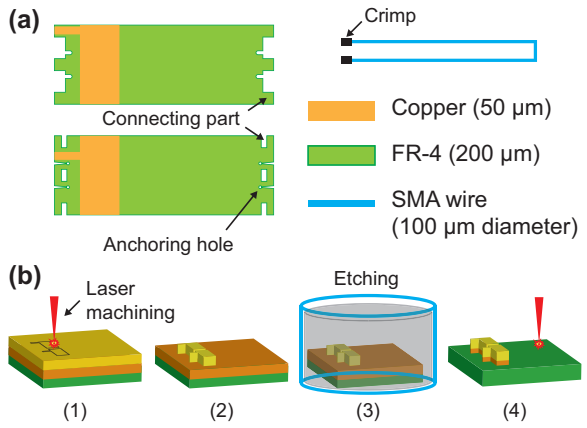

Fig. 4. (a) Components of SMA-based artificial muscle actuator: two compliant beams with electrode layer and SMA wire. (b) Fabrication process.

where r and l_e are the indicated distance and the length of the electrode as shown in Fig. 3a. Two electrodes are symmetrically attached to two beams.

Since $K'(k) = K(k')$, the complementary modulus k' are given by

$$k'_{in}(\theta) = \sqrt{\frac{\left((r+l_e)^{\pi/2\theta} - r^{\pi/2\theta}\right)^2}{\left((r+l_e)^{\pi/2\theta} + r^{\pi/2\theta}\right)^2}}, \tag{13}$$

$$k'_{out}(\theta) = \sqrt{\frac{\left((r+l_e)^{\pi/2(\pi-\theta)} - r^{\pi/2(\pi-\theta))}\right)^2}{\left((r+l_e)^{\pi/2(\pi-\theta))} + r^{\pi/2(\pi-\theta)}\right)^2}}. \tag{14}$$

Equations (3) and (7) are expressed as a function of the PRB angle (θ). The actuation displacement is coupled with the capacitance variation of integrated electrodes. Consequently, the relationship between the height of the actuator and the capacitance of two inclined electrodes can be obtained. Through a mathematical model, we confirm the feasibility of measuring the vertical displacement of the actuator.

D. Design of sensor-integrated SMA actuator

As shown in Fig. 3b and Fig. 3c, the horizontal contraction of the SMA wire by joule heating induces the vertical displacement of the actuator. To realize the amplification mechanism, anchoring holes are patterned in compliant beams so that the SMA wire can be routed to the desired path as shown in Fig. 4a. In addition, the SMA wire aligned along the dashed-line (Fig. 1a) is fixed through crimps as shown in Fig. 4a. The detailed design process of the actuator is described in previous research [7]. By deformation of the actuator, the configuration of two electrodes which are copper thin-film laminated on compliant beams is changed as shown in Fig. 3b. As explained in Section. II.C, the capacitance between two electrodes decreases when the vertical displacement of the actuator increases. Here, the sensor is composed of positive and ground electrodes. The upper side of the actuator

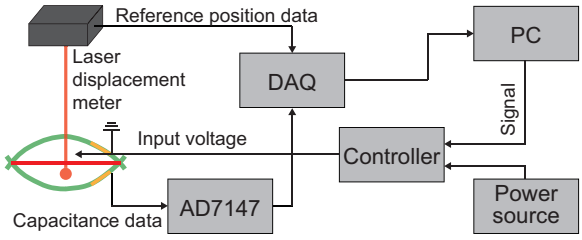

Fig. 5. Experimental setup for measuring reference and capacitance data and control of the actuator.

is generally exploited for task execution such as lifting the object, thus ground and positive electrodes are respectively located on the upper and lower side to minimize disturbance.

E. Fabrication process

As shown in Fig. 4b, the manufacturing process proceeds in five steps: the planar manufacturing process for the electrode layer in the order of (1) laser patterning for the mask layer, (2) peeling mask layer, (3) etching copper layer; (4) cutting a compliant beam along the designed pattern through laser machining; (5) integration process including SMA wire embedding, assembly of compliant beams, and wiring. The mask layer and compliant beams are cut by CO_2 (Universal Laser Systems) and UV laser (Oxford layer Ltd, UK) cutting system, respectively. Only the integration process requires manual handling. The copper-laminated FR-4 sheet (200 μm thickness) and SMA wire (Dynalloy) of 100 μm diameter are used for the compliant beam and actuation component. We used FR-4 as the compliant structure of the actuator due to its properties (a low density of 1.85 g/cm^3 and mechanical compliance) and the convenient fabrication process through laser machining. In this study, the usage of the copper-laminated FR-4 sheet can further enhance the convenience of the fabrication in that the compliant structure and electrode layer are integrated into a monolithic structure.

III. EXPERIMENTAL EVALUATION

A. Experimental setup, sensing capability, and calibration

An experimental setup is presented as shown in Fig 5. This setup consists of a capacitance-digit-converter (CDC) (AD7147, Analog Devices), a reference laser displacement sensor (HG-C1030-P, Panasonic), the developed actuator, data acquisition (DAQ) device (myRIO, National Instruments), a voltage controller, power supply, and one laptop. By using an experimental setup, we confirmed the verification of the theoretical design and sensing capability. In addition, calibration and transformation were conducted by measured data to control the actuator.

To verify the theoretical design, we measured the capacitance and reference displacement data for 10 cycles as shown in Fig. 6a. The initial capacitance is different between the model and experimental result since the theoretical model is an ideal case being only electrodes. On the other hand, the electrode in the experiment is physically and electrically connected to conductive materials and electronic devices. Therefore, the amount of change in capacitance between

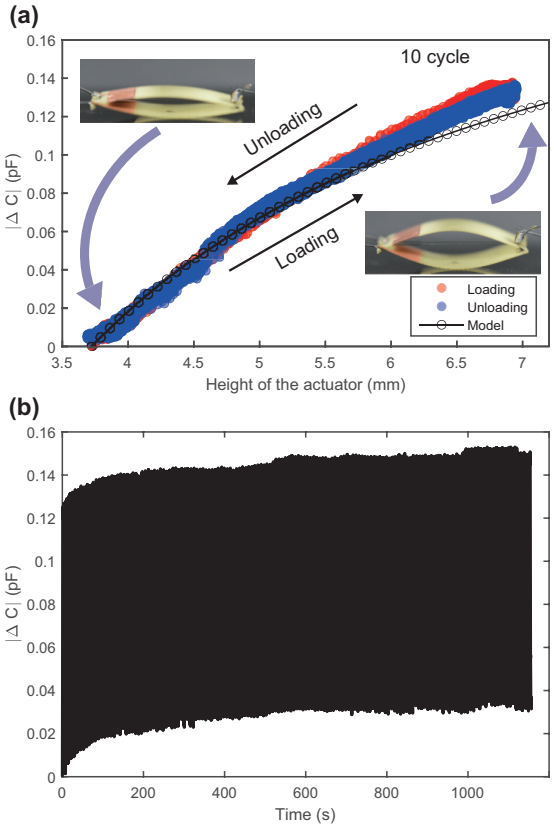

Fig. 6. (a) Capacitance vs. displacement profile. (b) cyclic test result

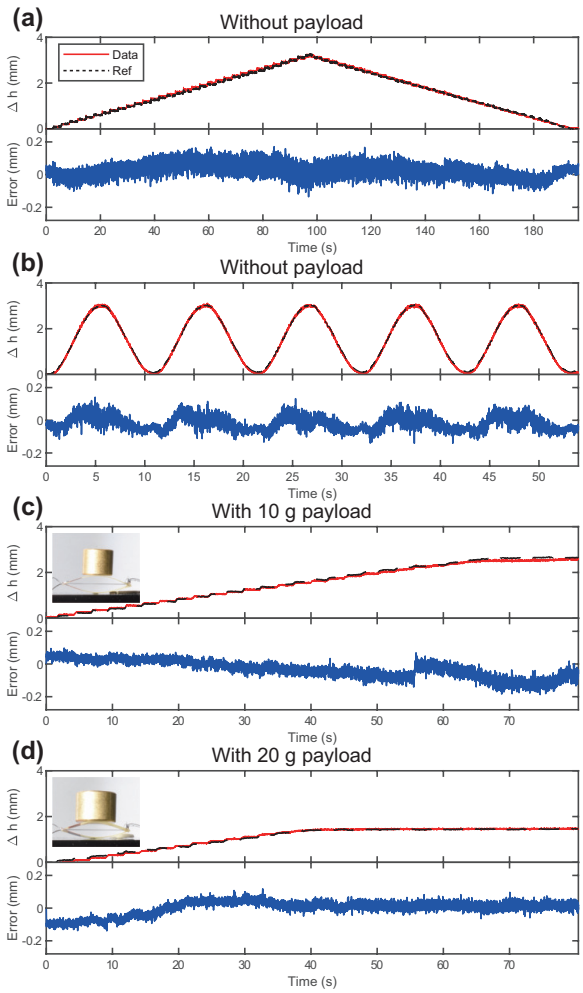

Fig. 7. Experimental results of step response control (a) without payload and with (b) 10 g payload and (c) 20 g payload, where Δh is the height variation from the initial height

model and experiment was compared. Fig. 6a shows that the experimental result approximates the model without hysteresis in the loading and unloading. In addition, we performed approximately 150 cycles of activation to confirm reliable data measurement in repeated actuation (Fig. 6b). In the cyclic test, the initial height of the actuator is shifted, which is an inherent characteristic of SMA caused by heat accumulation.

Based on the experimental result in Fig. 6a, the relationship between capacitance and reference displacement data can be analyzed. Since the variation of capacitance by changing the height of the actuator is nonlinear, the second order polynomial fit was performed, and the result is expressed by the following function:

$$f_1(x) = 2306 - 0.2028x + 4.457 \cdot 10^{-4} x^2 \qquad (15)$$

where $f_1(x)$ is the variation of the actuator height measured by the reference sensor and x represents the digitized capacitance data. By using this function, the height of the actuator is calibrated from the measured capacitance data. Therefore, a proportional integral derivative (PID) controller is used to control the vertical position (i.e., independent of the thermomechanical behavior of SMA) with capacitance change as a set point.

B. Experimental results

To confirm the controllability of the actuator, we conducted a control experiment with 100 μm step and sinusoidal response by using the measured capacitance data. Fig. 7 shows the transformed data from capacitance and reference data in all cases by varying payloads. In the case of the actuator without payload, an error between the two sensors is relatively large at maximum height, because the capacitance variation in this height is widely changed as shown in Fig. 6a. The root-mean-square errors (RMSE) of the actuator without payload are 0.05 (step) and 0.042 (sinusoidal) mm. In contrast, the initial height is shifted due to compliance of the structure as the payload is applied to the actuator. Since the calibration is not performed in the range lower than the initial position of the actuator, a step response is applied after initializing the height equal to the actuator without payload. The amount of error with a payload is similar to or lower than the actuator without a payload. RMSEs of the actuator with 10 and 20 g payload are 0.059 and 0.045 mm, respectively. Therefore, all datasets of the developed sensor are similar to reference displacement data, and experimental results validate sensing capability for realizing actuator control (even including a payload 90 times heavier than its weight).

TABLE I

SPECIFICATION OF THE PROPOSED ACTUATOR AND DEVICE

Specification	Value	Unit
Weight of actuator	0.22	g
Dimension of actuator	27 × 10 × 3.73	mm^3
Maximum stroke of actuator	3.23	mm
Average power density of actuator [7]	651	W/kg
Sensitivity of sensor	0.003-0.008*	mm/digit
Maximum tilting angle of mirror	20	degree

*: Corresponding with the actuation range

IV. DEMONSTRATION

A. 1-DoF mirror tilting system and mechanism

The prototype device is designed to maximize the advantages of the proposed actuator, which are high payload capacity and controllability. It is a suitable approach for operating a relatively large mirror compared with a MEMS mirror. The device is composed of the sensor-integrated SMA actuator, rotational stage, and mirror (2×2 cm) as shown in Fig. 8a. The stage (spring steel, 50 μm thickness) is fabricated by the laser machining. The flexure hinge of the stage is rotated by the vertical motion of the actuator (Fig. 1e). The motion of the actuator is converted to the rotational motion of the stage including the mirror. Fig. 1f shows the laser steering mechanism using the mirror. The larger mechanical angle allows for expanding optical scanning range.

B. Performance characterization

To estimate the angle of the mirror, the relationship between capacitance and stage height is utilized in the calibration. In the same manner as the actuator control performed earlier, the capacitance was transformed into position data via the second order polynomial fit as follows:

$$f_2(x) = 2756 - 0.2149x + 4.189 \cdot 10^{-6} x^2 \qquad (16)$$

where $f_2(x)$ is the variation of the vertical position of the stage measured by the reference sensor and x represents the digitized capacitance data.

Fig. 8b and 8c present the experimental result of measuring the position of the mirror through the actuator control. In this experiment, the 100 μm step and sinusoidal response are applied. The result of applying step response shows a similar profile for the only actuator control. On the other hand, in the sinusoidal response, the error occurs significantly in the initial state and the maximum height. RMSEs of step and sinusoidal response are 0.175 (1.218) and 0.114 (0.793) mm (degree), respectively. Table 1 shows the specifications of the actuator and device.

V. DISCUSSION & CONCLUSION

This paper describes the design, fabrication, and experimental evaluation of the capacitive sensor-integrated SMA actuator. By exploiting SMA and electrostatic capacitive sensing, we built an actuator that offered position control with a 20 g payload and a sensitivity of approximately 0.005 mm/digit with a weight of 0.22 g and dimensions of 27 × 10 × 3.73 mm. The proposed actuator has an additional sensing capability while maintaining the advantages of SMA. To leverage this actuator, we performed demonstrations of the meso-scale mirror tilting device, which steers the laser beam with step and sinusoidal response. In the future, we will conduct design optimization of the actuator and sensor for realizing the high-frequency operation of the mirror tilting device. In addition, we plan to minimize the noise and interference of capacitive sensors to embed multi-actuators into a 2-DoF mirror tilting device.

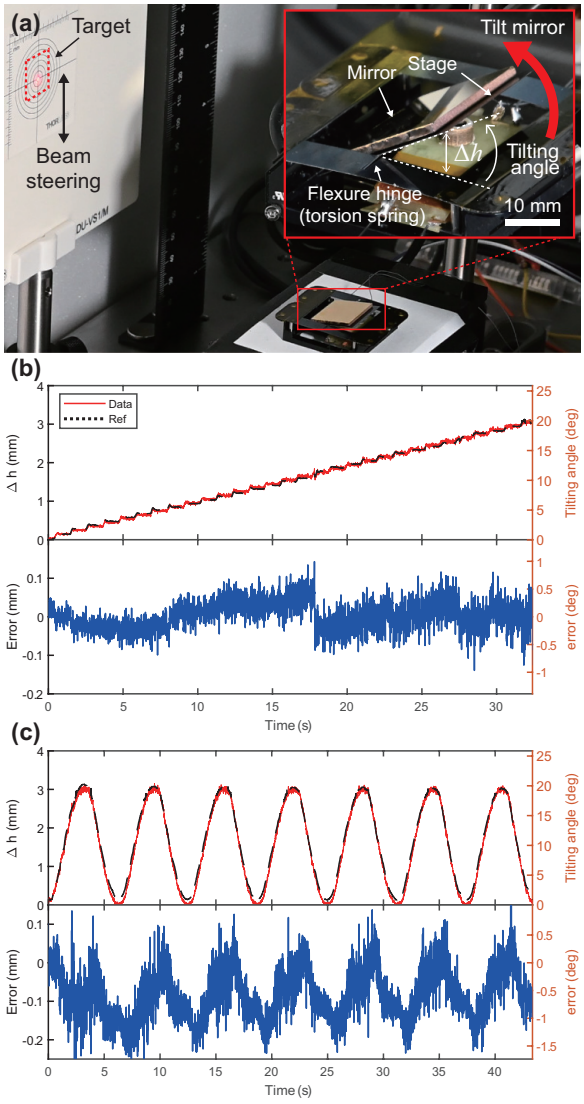

Fig. 8. Demonstration of laser beam steering (a) Experimental setup. Mirror tilting angle control of (b) 100 μm interval step response (c) sinusoidal response.

We anticipate that this actuator will be used in optical devices and micro-robotics in which high payload and sensing capability are required in restrictive form factors.

ACKNOWLEDGMENT

This work was supported by Basic Science Research Program through the National Research Foundation of Korea (NRF-2021R1C1C1011872).

REFERENCES

[1] J. Zhang, J. Sheng, C. T. O'Neill, C. J. Walsh, R. J. Wood, J.-H. Ryu, J. P. Desai, and M. C. Yip, "Robotic artificial muscles: Current progress and future perspectives," *IEEE transactions on robotics*, vol. 35, no. 3, pp. 761–781, 2019.

[2] Y. Chen, H. Zhao, J. Mao, P. Chirarattananon, E. F. Helbling, N.-s. P. Hyun, D. R. Clarke, and R. J. Wood, "Controlled flight of a microrobot powered by soft artificial muscles," *Nature*, vol. 575, no. 7782, pp. 324–329, 2019.

[3] J.-S. Koh, E. Yang, G.-P. Jung, S.-P. Jung, J. H. Son, S.-I. Lee, P. G. Jablonski, R. J. Wood, H.-Y. Kim, and K.-J. Cho, "Jumping on water: Surface tension–dominated jumping of water striders and robotic insects," *Science*, vol. 349, no. 6247, pp. 517–521, 2015.

[4] Z. Zhakypov, K. Mori, K. Hosoda, and J. Paik, "Designing minimal and scalable insect-inspired multi-locomotion millirobots," *Nature*, vol. 571, no. 7765, pp. 381–386, 2019.

[5] H. Suzuki and R. J. Wood, "Origami-inspired miniature manipulator for teleoperated microsurgery," *Nature Machine Intelligence*, vol. 2, no. 8, pp. 437–446, 2020.

[6] E. Leroy, R. Hinchet, and H. Shea, "Multimode hydraulically amplified electrostatic actuators for wearable haptics," *Advanced Materials*, vol. 32, no. 36, p. 2002564, 2020.

[7] D. Kim, B. Kim, B. Shin, D. Shin, C.-K. Lee, J.-S. Chung, J. Seo, Y.-T. Kim, G. Sung, W. Seo *et al.*, "Actuating compact wearable augmented reality devices by multifunctional artificial muscle," *Nature communications*, vol. 13, no. 1, pp. 1–13, 2022.

[8] N. Kellaris, V. Gopaluni Venkata, G. M. Smith, S. K. Mitchell, and C. Keplinger, "Peano-hasel actuators: Muscle-mimetic, electrohydraulic transducers that linearly contract on activation," *Science Robotics*, vol. 3, no. 14, p. eaar3276, 2018.

[9] J. Ueda, T. W. Secord, and H. H. Asada, "Large effective-strain piezoelectric actuators using nested cellular architecture with exponential strain amplification mechanisms," *IEEE/ASME transactions on mechatronics*, vol. 15, no. 5, pp. 770–782, 2009.

[10] D. J. Hartl and D. C. Lagoudas, "Aerospace applications of shape memory alloys," *Proceedings of the Institution of Mechanical Engineers, Part G: Journal of Aerospace Engineering*, vol. 221, no. 4, pp. 535–552, 2007.

[11] D. Stoeckel, "Shape memory actuators for automotive applications," *Materials & Design*, vol. 11, no. 6, pp. 302–307, 1990.

[12] J. M. Jani, M. Leary, A. Subic, and M. A. Gibson, "A review of shape memory alloy research, applications and opportunities," *Materials & Design (1980-2015)*, vol. 56, pp. 1078–1113, 2014.

[13] D. C. Lagoudas, *Shape memory alloys: modeling and engineering applications*. Springer, 2008.

[14] J.-s. Koh, "Design of shape memory alloy coil spring actuator for improving performance in cyclic actuation," *Materials*, vol. 11, no. 11, p. 2324, 2018.

[15] M. Sreekumar, T. Nagarajan, M. Singaperumal, M. Zoppi, and R. Molfino, "Critical review of current trends in shape memory alloy actuators for intelligent robots," *Industrial Robot: An International Journal*, 2007.

[16] C.-C. Kim, H.-H. Lee, K. H. Oh, and J.-Y. Sun, "Highly stretchable, transparent ionic touch panel," *Science*, vol. 353, no. 6300, pp. 682–687, 2016.

[17] C. M. Boutry, M. Negre, M. Jorda, O. Vardoulis, A. Chortos, O. Khatib, and Z. Bao, "A hierarchically patterned, bioinspired e-skin able to detect the direction of applied pressure for robotics," *Science Robotics*, vol. 3, no. 24, p. eaau6914, 2018.

[18] U. Kim, D.-H. Lee, Y. B. Kim, D.-Y. Seok, and H. R. Choi, "A novel six-axis force/torque sensor for robotic applications," *IEEE/ASME Transactions on Mechatronics*, vol. 22, no. 3, pp. 1381–1391, 2016.

[19] P. Puangmali, K. Althoefer, L. D. Seneviratne, D. Murphy, and P. Dasgupta, "State-of-the-art in force and tactile sensing for minimally invasive surgery," *IEEE Sensors Journal*, vol. 8, no. 4, pp. 371–381, 2008.

[20] L. L. Howell, "Compliant mechanisms," in *21st century kinematics*. Springer, 2013, pp. 189–216.

[21] Y. Xiang, "Further study on electrostatic capacitance of an inclined plate capacitor," *Journal of Electrostatics*, vol. 66, no. 7-8, pp. 366–368, 2008.